Nanomechanics and Laser-Induced Damage in Optical Multilayer Dielectric Gratings

Introduction

Multilayer dielectric (MLD) pulse-compressor gratings are critical components used in a high-peak-power laser system's amplification system and have been a focus of recent research and development efforts because of their low damage thresholds.[1,2] At LLE, the peak-power capability—and, therefore, the overall performance of the petawatt-class OMEGA EP Laser System—is limited by the laser-damage resistance of diffraction gratings in the chirped-pulse–amplification (CPA) pulse compressors for each beamline.[3–6] Increasing the damage thresholds of these components is, therefore, an important objective.

A low-temperature chemical cleaning approach developed by Howard *et al.*[7] to improve the performance of these MLD gratings has demonstrated that grating coupons that were cleaned using the optimized method consistently met OMEGA EP requirements on diffraction efficiency (>97%) and 1053-nm laser-damage resistance at 10 ps (>2.7 J/cm^2). They also observed that, for samples with the highest damage threshold, there were minimal laser-conditioning effects, suggesting a transition from a contamination-driven laser-damage mechanism to defect-driven damage for well-cleaned components. Hereafter, this metric—laser-induced–damage threshold (LIDT)—will be referred to as optical testing. Such optical testing is the most common way to characterize the performance and, therefore, the quality of an MLD grating that has been cleaned for use in a high-power laser system.

There is some concern that cleaning procedures and/or fabrication techniques for gratings can mechanically weaken the fragile grating pillars, possibly affecting the grating's resistance to laser damage and, therefore, warrant mechanical characterization. The development of a methodology to monitor a grating's mechanical properties will enable one to better understand the fabrication and cleaning processes and will point to appropriate modifications that will preserve or enhance the grating's integrity.

Nano-indentation of MLD gratings[8] is our adopted approach, and the indents that invoke fracture of the silica walls are treated in detail. Nano-indentation and/or uniaxial compression of patterned surfaces manufactured by techniques such as focused ion-beam (FIB) milling and lithography[9] have shown tremendous potential in isolating the ductile response of the material from its brittle response. These studies prominently feature the uniaxial compression of metallic high-aspect-ratio micro- and nanopillars,[10–13] produced by FIB milling, with diameters ranging from 75 nm to 7.5 μm. Such structures are used to study the ductile deformation of metals, specifically size effects and their dependence on properties such as yield strength.

Experiments on micropillars of amorphous silica subjected to uniaxial compression have recently been reported by Lacroix *et al.*[14,15] Their findings indicate that silicate glasses are very suitable for micropillar compression because the ratio of the yield stress to Young's modulus is comparatively high compared to a typical metal. They also demonstrated the experimental conditions under which plastic flow can be obtained in compression of these pillars without catastrophic failure and accompanied only by minor, well-defined radial crack patterns.

The LIDT of amorphous silica gratings for ultrahigh intensity laser systems has been studied extensively in literature.[16,17] The electric field is known to be maximum at the top area of the grating walls. It is in this region of local enhancement that damage initiates, defining the ultimate damage threshold.

Both tests (laser-induced damage and nano-indentation), although vastly different in nature and implementation, inherently measure the performance of the grating (optical versus mechanical). Fracture, caused by a concentration of mechanical stresses, is an integral part of these measurements. Therefore, it is imperative and almost intuitive to explore mechanical testing (nano-indentation) as a means to complement and even precede optical testing to establish the "quality" and performance of an MLD grating sample. We are guided by the observation that both optical fields (electric and magnetic) and mechanical fields (stress and strain), when interacting with the grating

geometrical features and with defects and inhomogeneities, will show significant concentrations.

Materials and Methods

1. Fabrication of MLD Gratings

The process of manufacturing MLD gratings has been detailed extensively in published literature[7,8,18] and is summarized here for completeness.

The first step is to deposit the MLD coating on the glass substrate (fused silica or BK7) by reactive evaporation at 200°C as a thick, modified-quarter-wave thin-film stack[19] with hafnia (HfO_2) and silica (SiO_2) used as the high- and low-index materials, respectively. Next, a bottom antireflective coating (BARC) layer (organic polymer) may be applied to the multilayer mirror, followed by a layer of photoresist coating. Interference lithography is used to pattern the grating (grooves, 1740 lines per mm). Once patterned, etching is performed to remove the BARC and a portion of the top MLD layer, leaving the silica wall geometry.

Finally, organic (BARC, photoresist layers, etch products, and environmental contamination) and inorganic residues (metallic contaminants) are stripped away in a final cleaning process. For the grating samples used in this work, the silica walls were ~440 nm high with a slightly tapered geometry (~250 nm wide at the base and ~150 nm wide at the top).[8]

2. An Optimized Procedure for Cleaning MLD Gratings to Maximize Laser-Damage Thresholds

For this study, cleaning experiments were performed on small-scale MLD grating coupons. Round hafnia/silica MLD gratings (100 mm in diameter, 3 mm thick) were broken into eight equally sized, wedge-shaped coupons. All cleaning experiments described in this section were performed on uncleaned gratings with BARC and photoresist still intact (that is, they were not subjected to any photoresist stripping or cleaning operations other than those described here). Uncleaned gratings can be easily distinguished by their characteristic brown and hazy appearance (which disappears when a grating is well cleaned), attributed to the residual organic materials.

Acid piranha, the most widely used chemical cleaning agent at higher temperatures,[18] was insufficient for our low-temperature (40°C) process; a multistep technique is warranted to ensure a wide-range removal of performance-limiting contaminants. This cleaning methodology—discussed in Howard's work[2,7,8,18–20] and adapted by improvising on existing literature for cleaning gratings (such as Refs. 18 and 21) and semiconductor wafer processing—was split into two parts: a partial clean consisting of six steps and a final clean that included a plasma step. The cleaning process is summarized in Table 146.II.

The final clean, which is a third plasma treatment, can be either an air plasma[7] or an oxygen plasma (conventionally used

Table 146.II: Cleaning process for the MLD gratings used in this work.

Cleaning Process				Process Steps	
	Step	Temperature (°C)	Time (min)	Chemical	Purpose
Partial clean	1	40	15	5:1 piranha spray	Strip photoresist and etch residues
	2	40	15	2:1 piranha spray	Strip photoresist and etch residues
	3	23	10	Air plasma (6.8-W power)	Completely remove BARC
	4	40	10	1:1:6 SC-2 no-stir soak	Remove metallic contamination
	5	23	10	Air plasma (6.8-W power)	Remove light organic matter
	6	23	5	2800:1 BOE* soak	Reduce grating duty cycle
Final step	7	23	15	Air plasma (6.8-W power) OR Oxygen plasma (6.8-W power)	Remove organics from grating surface

*buffer oxide etch

in grating cleaning procedures). As shown later, this choice can have a decisive effect on the laser-damage threshold attained by a grating sample.

3. Laser-Damage Testing

Damage testing was carried out at LLE's damage-testing facility on the short-pulse (10-ps) system with operating capabilities in both air and high vacuum (4×10^{-7} Torr). The MLD grating samples studied here were tested in air using *s*-polarized light at 1053 nm at an incident beam angle of 61° with an irradiation spot size of 370 μm (e^{-1} in intensity) in the far field. Beam analysis and fluence calculations were performed using the Ophir–Spiricon commercial laser-beam profiler. Laser damage was assessed *in situ* using a white-light imaging system (~100× magnification). Damage was defined as a feature on the sample's surface that was not observed before laser irradiation.[20,22] Damage thresholds are reported as beam-normal fluences. An example of a damage site on grating 566-5 is shown in Fig. 146.22.

Our damage tests employed the *N*-on-1 testing regime performed in air. Particulars of this testing protocol and others, such as 1-on-1, can be found in literature.[23] *N*-on-1 (stepwise ramped fluence) testing is conducted by irradiating the sample site at a fluence that is well below the 1-on-1 threshold for ten shots. If no damage is detected, the same site is irradiated with five more shots at a slightly increased fluence. This is continued until damage is observed in white light, at which point the damage onset fluence is recorded as the *N*-on-1 threshold for that site. The *N*-on-1 test is repeated for five sites on each MLD grating sample to generate an average and a standard deviation, which are reported as the *N*-on-1 threshold and measurement error, respectively.

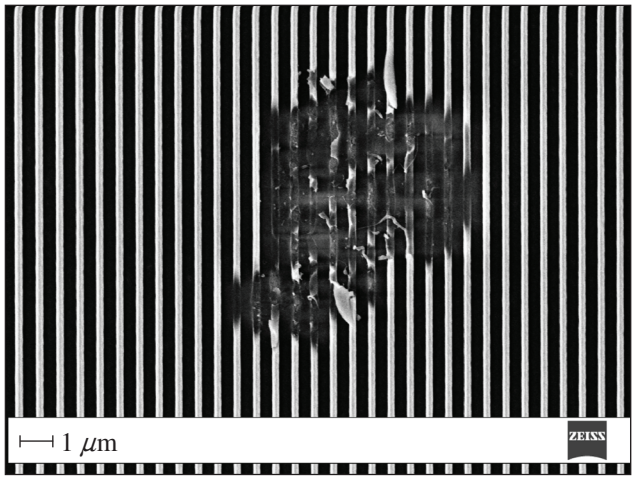

G10719JR

Figure 146.22
A scanning electron microscope (SEM) image of an *N*-on-1 laser-induced–damage site on the multilayer dielectric (MLD) grating structure.

4. Nano-Indentation of MLD Gratings

An MTS Nanoindenter XP fitted with a conical tip (60° included angle, 1-μm tip radius) was used in this work. The system was calibrated by performing nano-indentation on fused silica. Because of the limited imaging capabilities of the instrument and given the submicron scale of the pillar structures, it was not possible to resolve the impressions made by the indenter using the nano-indenter's built-in microscopy; instead, the sample had to be transferred to a scanning electron microscope (SEM) to observe the indents and "wall" damage. Loads in the 0.1- to 0.5-mN range were used and three types of indents could be produced by simply displacing the location of the indentation tip on the grating: centered, partially off-centered, and mostly off-centered indents.

Experimental Results

1. LIDT Results for Gratings and Cleaning Processes

In this study, the fabrication method of gratings was the same across the three samples: 13P-11-56/#566-3, 13P-11-56/#566-5, and 5P-12-56/#644-1. The cleaning procedures detailed earlier were used to prepare these gratings before they were subjected to laser-damage testing. The details of the cleaning methods for our samples are included in Table 146.III. Hereafter, for purposes of brevity, the grating samples will be addressed as #566-3, #566-5, and #644-1.

Two of the gratings (#566-3 and #566-5) that originated from the same coating run were processed together until the cleaning step. The third grating specimen (#644-1) was fabricated a year later using an identical coating process (5P-12-56).

Table 146.III: Summary of LIDT results for gratings and specific cleaning methods used.

Grating	Cleaning Process	Diffraction Efficiency Results (%)	*N*-on-1 LIDT (J/cm^2); air
13P-11-56/#566-3	Partial + air plasma	97.3±0.2	3.66±0.51
13P-11-56/#566-5	Partial + O_2 plasma	97.3±0.5	4.30±0.25
5P-12-56/#644-1	Partial + O_2 plasma	97.9±0.5	1.82±0.08

2. Nano-Indentation Data and Grating Brittleness

Nano-indentation tests were performed on all three grating samples at loads of 0.1, 0.2, 0.3, 0.4, and 0.5 mN. For each sample and at each load, nine indents were made at locations several microns apart. The aim here was to make as many decentered indents as possible. As mentioned in detail elsewhere,[8,24] the centered indents are useful in measuring the yield strength of silica at nanoscale corresponding to this unique geometry. Conversely, off-centered indents are inherently related to fracture of the grating walls, which can now be used to explore a connection with LIDT (associated with fracture as well). This is shown in Fig. 146.23.

Therefore, after performing indentations on the samples, we analyzed each corresponding load-displacement curve to separate the off-centered indents from the centered ones. An example for #566-5 indented at a load of 0.2 mN is shown in Fig. 146.24. The load-displacement curves make a clear distinction between centered and off-centered indents. The centered indent looks similar to an indent in a bulk material[8,24] and has no wall fracture associated with it. The difference, however, from bulk nano-indentation is that in bulk nano-indentation the surrounding material laterally constrains the material deformation. In grating ("wall") nano-indentation, such lateral constraint is reduced because of the small thickness of the silica wall. The other two curves, showing the off-centered indents, include fracture that is seen by the sudden break in the curve (leading to a "plateau") followed by additional loading.

For the purpose of extracting a metric that can be useful in analyzing the mechanical performance of gratings, which can then be compared to their optical performance (LIDT), we located the point of fracture initiation for each of the load-displacement curves. This is illustrated in Fig. 146.25 for grating #566-3 at a load of 0.2 mN. The location of the fracture initiation point (penetration depth Δ) for each indent depends on the amount of decentering; naturally, this is different for each indent (see Fig. 146.25). To evaluate the grating as a whole at

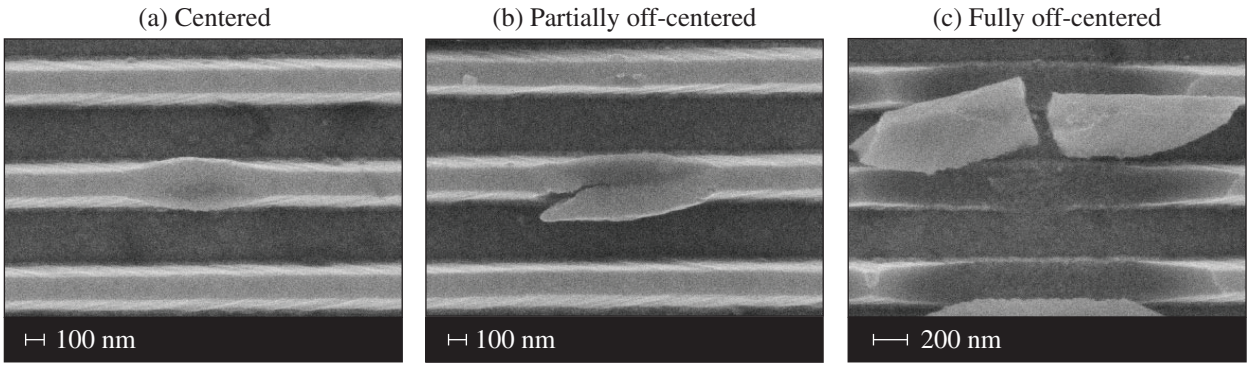

Figure 146.23
Three distinct nano-indentation responses are seen in MLD gratings.

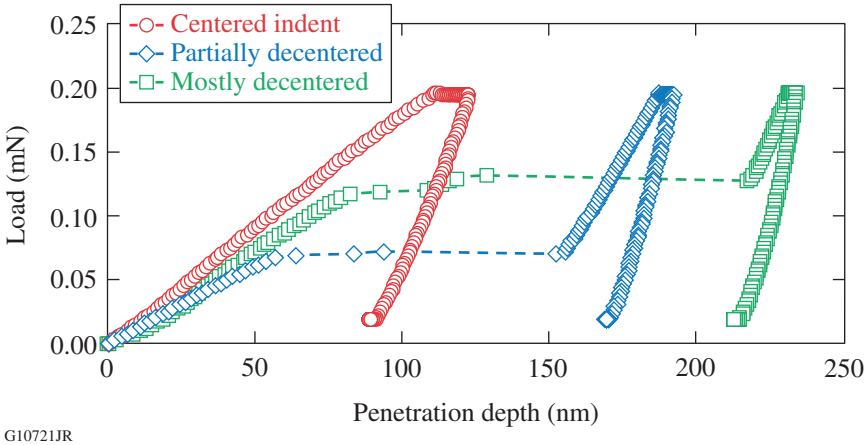

Figure 146.24
Load-displacement curves of nano-indentation for grating #566-5 with a 0.2-mN load.

that particular load, however, we chose the smallest penetration depth across all indents to represent the value at which fracture is initiated. In this example (Fig. 146.25), a penetration depth of 81 nm is the weakest site for failure under a nanomechanical load of 0.2 mN and will be designated as Δ_{min}. Similarly, data can be collected across all three grating samples for a load range of 0.2 to 0.5 mN.

We considered only those indents made at loads varying from 0.2 to 0.5 mN since indentations made at the 0.1-mN load did not yield any discernible instances of fracture.

3. Brittleness, Deformation, and LIDT

The penetration depths corresponding to the weakest sites for fracture initiation (Δ_{min}) at each load and sample are plotted against the measured values of LIDT in Fig. 146.26.

Using the methodology discussed in literature[8] based on the geometry of the grating walls (width at the top of the wall, $w \sim 150$ nm) and contact area a (function of radius of indenter R and load applied P) defined at the time of initiation of fracture corresponding to Δ_{min}, we can determine the yield "strength" of the grating and plot it against measurements of LIDT. The yield strength is a stress found for the maximum load and the impression area. The contact area radius a is found by

$$a = \sqrt{2R\Delta_{min}} \tag{1}$$

and the corresponding uniaxial yield strength by

$$\sigma_Y = \frac{P}{2aw}. \tag{2}$$

The extracted yield stress is correlated to the LIDT in Fig. 146.27.

4. Geometrical Discontinuities and Surface Heterogeneities

The MLD gratings, after cleaning treatments, are observed to have a distinctive type of surface defect as seen in SEM images—disfiguration along the top of the wall (also referred to as "undulations").

Observations from several SEM images such as the ones shown in Fig. 146.28 reveal a direct correlation between the

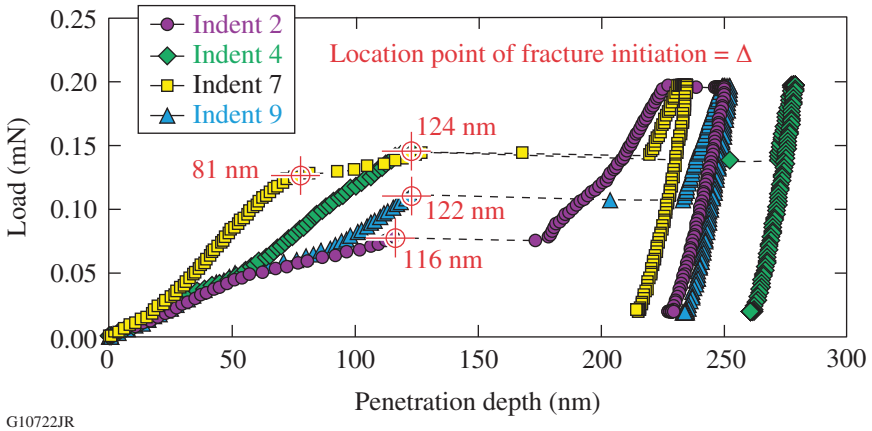

Figure 146.25
The location of fracture initiation is measured using the load-displacement curves for off-centered indents made on MLD grating #566-3 with a 0.2-mN load.

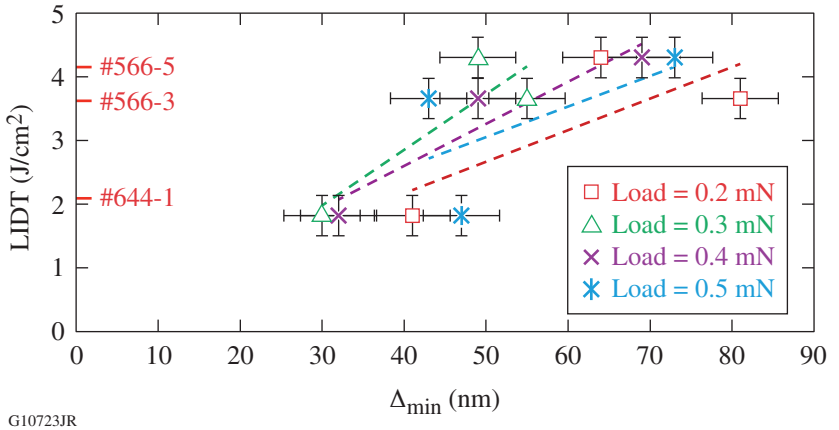

Figure 146.26
Relationship of laser-induced–damage threshold (LIDT) and the minimum depth of penetration into the MLD grating needed to initiate fracture.

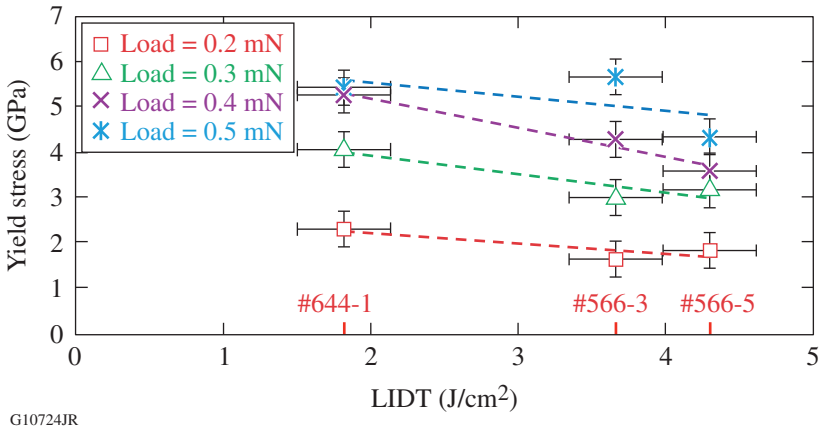

Figure 146.27
Relationship of LIDT and the extracted yield stress.

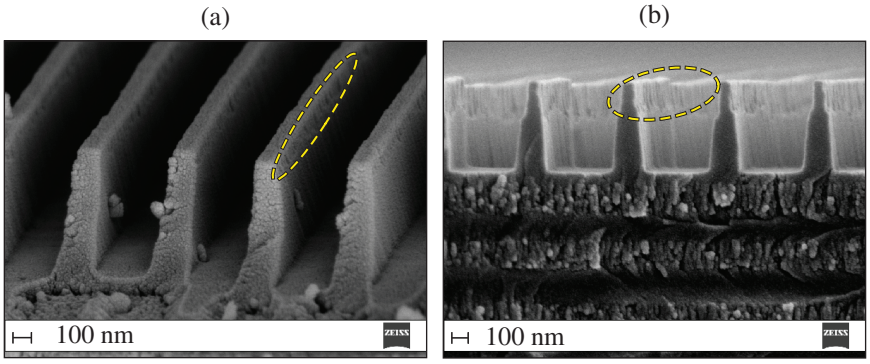

Figure 146.28
Severity of the undulations on the grating walls are related to the measured LIDT.

sizes of the undulations, seen as disfigurement at the top of the grating walls [circled in Figs. 146.28(a) and 146.28(b)], and the measured LIDT. Stronger undulations are associated with gratings that performed poorly in the optical testing, yielding lower values of laser-damage thresholds. Such surface defects (numerically modeled in the next section) are expected to play an important role in determining the quality of a particular grating since they would concentrate electric fields and mechanical stresses associated with nano-indentation. Therefore, they are an important consideration to our experiments.

These defects are thought to be regions of concentration of both mechanical and optical fields and are, therefore, important features to be included in our numerical modeling.

Numerical Simulations

For the numerical simulations, we used the commercial finite element package ABAQUS® (version 6.14-1). Guided by 2-D finite element analysis (FEA) performed previously,[8,25] the nano-indentation experiment was modeled as a 3-D problem using hexagonal, eight-node linear brick elements for the grating structure. The indentation region was significantly smaller than the size of the sample modeled; therefore, this area of large deformation was modeled using a highly refined mesh as compared to regions surrounding it.

The grating structure is defined as an elastic–plastic material composed of silica with an underlying layer of hafnia (~130 nm). The elastic modulus of silica was selected as 95 GPa (Ref. 26) and a Poisson ratio of 0.17. Isotropic hardening was implemented to model plasticity in the material corresponding to a yield stress of 2.8 GPa (based on the work described in Chap. 4 of Ref. 25). Hafnia was modeled as an elastic material with a Young's modulus of 130 GPa and a Poisson ratio of 0.25 (Ref. 26). The indenter tip (~1400-GPa diamond, elastic modulus) was modeled as an analytical rigid body since we did not expect it to deform during the experiment.

The nano-indentation problem was set up for simulation in four different ways as seen in Fig. 146.29. Since the purpose of this work is to correlate optical and mechanical damage fields in grating testing, we will mainly consider simulations of off-centered indents—namely the 25%, 50%, and fully decentered models (details of the centered model are discussed elsewhere[8,25]). Our goal is to simulate the nano-indentation testing. These analyses can then be used

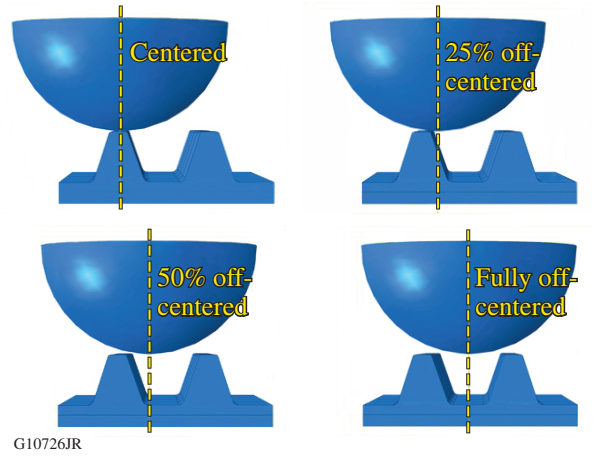

Figure 146.29
The ABAQUS® simulations were run using four setups to represent "centered" and "off-centered" indents.

to evaluate the different regions in a grating structure where stresses are concentrated.

1. Simulation of Off-Centered Nano-Indentation

We have observed (Sec. 4.3.1 of Ref. 25) that a high degree of indenter tip off-center coupled with a relatively deep penetration depth (≳150 nm) of indenter tip corresponds to catastrophic indents on the grating structure. Such "slightly"-to-"mostly" off-centered indents include effects of both ductility and brittle deformation.

Figures 146.30(a)–146.30(d) show the evolution of localized deformation and damage for a 50% decentered indent as the depth of penetration of the indenter tip is increased from 50 nm to 250 nm. The regions of highest concentration of maximum principal stress are seen in the regions of the grating wall that are "stretched" at lower penetration depths. As greater penetration depths of 170 nm and 250 nm are reached, the highest concentrations of maximum principal stress also extend to the adjacent wall since it is also now in significant contact with the indenter tip. This not only causes both the walls to stretch excessively but also affects the "foot" of the wall, which is found to concentrate maximum principal stress. It should be noted here that we have not modeled crack growth in this simulation; therefore, it is highly likely that excessive stretching seen in off-centered indents corresponding to high depths of penetration would indeed fracture the silica walls. In summary, the sequence of events in off-centered indentation consists of mechanical stretching of the grating top, followed by load shearing with neighboring pillars and load transmission to the base of the grating.

2. Simulation of Geometric Discontinuities

The 3-D simulations discussed previously assume that the shape of the grating is rectilinear. We now take into account some of the inhomogeneities that are encountered with gratings that can potentially act as regions to concentrate mechanical stresses in a nano-indentation test and have a direct impact on its laser-damage threshold.

The off-centered nano-indentation experiment is now modeled as a plane-strain simulation in 2-D and is meshed using four-node bilinear plane-strain quadrilateral elements. Highly refined meshing is used near the area of contact with a progressively coarser mesh away from the zone of maximum deformation (grating walls and the top few layers of the grating). The grating structure is modified to include the effects of thickness

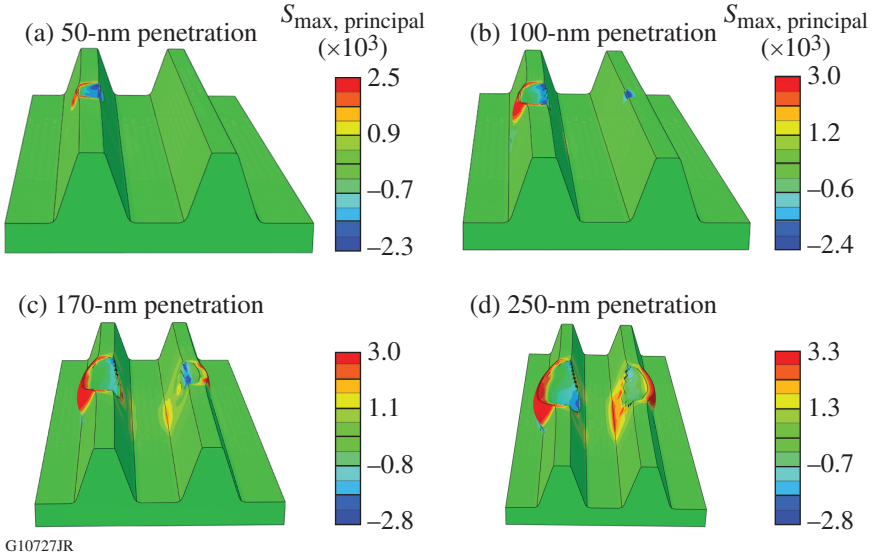

Figure 146.30
Damage is restricted to a single wall for penetration of 50 nm but extends to the adjacent wall as the penetration increases, eventually leading to fracture (stress is given in MPa).

discontinuity evident as disfigurement of the grating walls (undulations shown in SEM images in an earlier section). The results from the simulation are compared to those from an ideal grating structure and illustrated in Figs. 146.31(a) and 146.31(b).

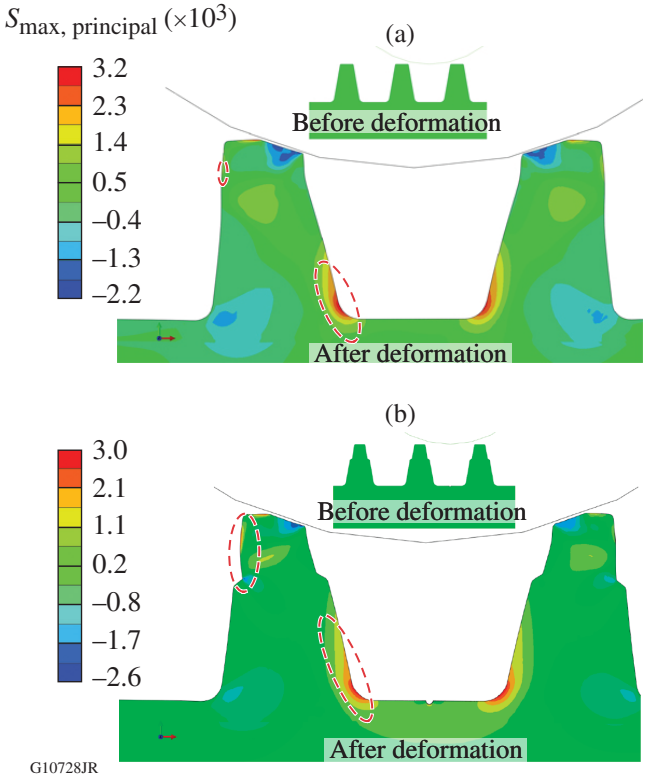

Figure 146.31
Comparison of (a) an ideal grating (no defects) with (b) a disfigured grating simulated for a penetration depth of 50 nm.

It is evident that, for a penetration depth of only 50 nm, the "disfigured" grating concentrates maximum principal stresses at the foot of the grating wall as well as along the undulation (peak stress ~3 GPa), whereas there is no significant accumulation of stresses along the wall of the ideal grating shape.

In addition to the stress concentration along the foot of the grating, the thickness discontinuity includes an additional effect, reminiscent of concentrated plastic shear deformation (shear banding).

The plastic strain (maximum principal component) for ideal and disfigured gratings at a penetration depth of 50 nm is plotted in Figs. 146.32(a) and 146.32(b), respectively. This helps to further assess the areas of the grating structure that are exposed to stress concentration in a nano-indentation test. It is seen that there is a "banding" effect in the upper region of the grating

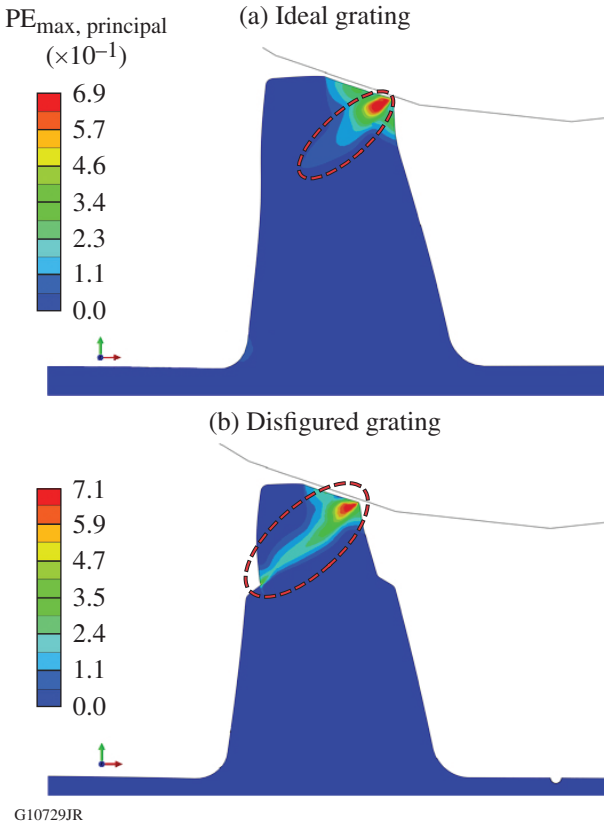

Figure 146.32
(a) A shear band caused by the plastic strain is prominent only in the area of contact with the indenter tip. (b) The shear band for the ideal shape is prominent in the disfigured grating and extends across the top width of the grating wall.

wall where it makes contact with the indenter tip. This "band," or the region under plastic strain, is significantly evolved in the disfigured grating as compared to the ideal grating structure.

We have also modeled nanometer-sized porosity at the grating "floor." A 100-nm pore is shown in Figs. 146.30(b) and 146.31(b). Such pores also concentrate tensile mechanical stresses, exactly as they concentrate electrical fields[27–30] by enhancing localized absorption effects.[31]

Discussion

1. Effect of Cleaning Procedures on LIDT

The cleaning procedure is widely reported to have a significant impact on the damage threshold of these pulse-compression gratings.[18,20] Extensive research dedicated to studying the effects of various cleaning processes (Piranha at different temperatures, Nano-Strip)[9,32–36] on the threshold at 10 ps, 1053 nm shows that the efficiency of the process (measured by reduction in traces of photopolymers and organic contaminants after cleaning) is linked to the LIDT measured for the grating.

For our purposes, subtle differences in the cleaning processes (shown in Table 146.III), such as using air plasma over oxygen plasma, cause significant changes in the measured LIDT for the respective gratings. Specifically, this is the only difference between gratings #566-3 and #566-5 (which were processed identically until this point), and yet the latter performed much better in optical testing (LIDT 4.3±0.25 J/cm^2). The same is true in comparing #566-3 and #644-1. Therefore, it must be emphasized that, although these differences in cleaning procedures might seem insignificant, they lead to critically different optical performances.

It must also be noted that although we have shown that changes in cleaning methods have led to vastly different values of measured LIDT, this is not the main purpose of this study, and they are discussed elsewhere.[2,7,20]

2. Thickness Undulation and Concentration of Mechanical Fields

Guided by SEM images (in Fig. 146.28) and LIDT data, an apparent relationship between the shape of the top of the grating wall and the optical performance of the grating can be summarized as follows:

- Undulations can amplify electric-field intensification in those regions, leading to higher damage probability.

- Two-dimensional finite element analysis shows higher stress concentrations and shear band development in a disfigured grating for the same ~50-nm penetration depths.

The primary purpose of the 3-D simulation was to identify the regions of the grating structure that are affected in a nano-indentation test and then use these regions to compare nano-indentation to the results from a laser-damage–threshold test. Specifically, for a 50% off-centered indent, Fig. 146.30 shows that the highest levels of maximum principal stress are concentrated in the stretched part of the wall at lower levels of penetration depth. This region can be thought of as the site of fracture initiation in the nano-indentation experiment.

The indentation depth at which the maximum principal stress exceeds the fracture stress of silica corresponds to the location of the point of fracture initiation (compare to Δ_{min} indicated in load-displacement curves; see Fig. 146.25). The numerical simulations (Fig. 146.30) indicate that this indentation depth is in the 50-nm to 100-nm range, which corresponds well with experimental data. As indentation depths increase, fracture becomes imminent and is suggested by the spatial increase in stretched regions of the grating wall (near the top) as well as adjoining areas where stress is concentrated—the stretched region in the adjacent grating wall and foot of the grating.

It is widely reported in literature[16,17,19,37,38] that in a laser-damage–threshold test, the damage to the MLD grating appears to start at the upper edge of the silica walls—where the modulus of the square of the electric field is highest.[16,17] SEM images of our gratings (Fig. 146.28) after cleaning show distinctive disfigured regions at the top of the grating wall, which in some cases have thinned the gratings to a great extent. Guided by these SEM images and LIDT data, there is an apparent relation between the shape of the top of the grating (or, severity of undulations created) and the respective values of damage threshold measured in optical testing. Gratings with smaller degrees of thickness disfigurement are associated with higher values of laser-damage thresholds. Any inhomogeneity along the top of the grating wall will amplify the catastrophic effects of the laser energy used to irradiate these gratings.

Having established that analyzing these undulations is an important aspect of understanding why gratings behave differently in LIDT, we can now discuss how nanomechanical testing of these silica walls can be used to understand their performance. For a penetration depth of 50 nm, it is observed in the 2-D finite element model that the two highlighted regions in the figure for the ideal [Fig. 146.31(a)] and disfigured [Fig. 146.31(b)] grating concentrate the highest levels of (tensile) maximum principal stress. Based on the area around the top of the grating wall, it is clear that for a given penetration depth, the disfigured grating experiences much higher levels of stress (~2.5 GPa) as compared to an ideal grating in the same region (<1 GPa). This shows that mechanical stresses are amplified greatly for a disfigured grating, and, as the severity of undulations increases, it can be expected that stresses would also increase, ultimately leading to a mechanical failure of the grating wall.

Plastic strains are also useful in understanding deformation of these gratings, and it is seen that during the nano-indentation test, a "shear band" develops as contact proceeds. Figures 146.32(a) and 146.32(b) compare the shear bands of ideal and disfigured grating structures, respectively. Clearly, the banding effect is more severe in the case of the grating with an undulation and extends across the width of the wall along the region where it is disfigured. Strains as high as 45% are seen in regions away from the contact area and are highlighted in the figure. The shear band in the ideally shaped grating is contained mostly within the area that is in contact with the indenter tip.

It must also be noted that the penetration depth chosen here (50 nm) to model the nano-indentation stresses in the grating is similar to the values of Δ_{min}, from the load-displacement curves, which represents the point of fracture initiation. Therefore, it can be inferred that under nanomechanical testing, the gratings with more-severe undulations will fracture before gratings that are relatively free of these features. This result is critical in explaining why gratings with a lower Δ_{min} have a lower LIDT (shown in Fig. 146.26). We also note that these simulations highlight that a nanomechanical test exposes regions of the grating structure that are impervious to its laser-threshold performance statistics.

3. Correlation of Optical and Mechanical Tests (LIDT and Δ_{min})

Figure 146.26 shows LIDT for the three differently cleaned gratings against Δ_{min} at various loads used to measure the nano-indentation. It is apparent that there is a strong linear dependence of Δ_{min} on the measured LIDT (J/cm^2). LIDT increases with increasing values of Δ_{min}; that is, the more "brittle" a grating, the lower its damage threshold. This correlation is novel and important for two different reasons. First, it provides us with a quantitative metric that can be used to predict optical performance of gratings based on nanomechanical tests alone. Simply put, a grating that shows an earlier initiation of fracture in an off-centered nano-indentation test (tracked using load-displacement curves) has a greater likelihood to be associated with a lower LIDT value as compared to a grating that could absorb more mechanical stress before fracture initiation. Second, this result can also be extended to correlate yield stress in these gratings (at the time of first fracture) to their respective laser-damage thresholds. The relation of LIDT and yield stress in Fig. 146.27 indicates that a grating with a higher LIDT will have a lower value of yield stress. This means that for decreasing yield strength, the grating is more ductile or can absorb more mechanical energy before it fractures. In summary, gratings with higher ductility demonstrate higher LIDT.

It is also worth noting from Fig. 146.26 that the correlating lines, when extended, have intercepts near zero. Of course, all gratings have a nonzero LIDT; however, this observation indicates that, if the deflection Δ_{min} to fracture is practically nil, the resulting LIDT also vanishes. Such a correlation of fracture and LIDT is in agreement with the discussion in this section.

We will now discuss first-principles–based dimensionless metrics for correlating our results between nano-indentation and optical performance. Our goal is to cast our results in a way that may extend their range of validity to experimental conditions, other than the ones we have used here. In essence, we are seeking appropriate ways to cast our experimental results in a dimensionless form.

Higher ductility in grating structures can be considered in terms of stretched zones as indicated in finite-element simulations [Fig. 146.30(c)]. This stretching before fracture initiation in an off-centered indent is attributed to the (tangential) stress (hoop) exerted by the indenter. This phenomenon is broadly analogous to an internally pressurized cylinder. The pressure causes the cylinder to expand or stretch and we can calculate a hoop strain ($\varepsilon_{\theta\theta}$) associated with it. The fracture strain is calculated for the penetration depth (Δ_{min}) at which stretching leads to fracture initiation and also depends on the indenter's radius and the grating pitch.[25] We can now normalize Δ_{min} by the hoop strain ($\varepsilon_{\theta\theta}$).

We also need to normalize LIDT's to some nominal threshold fluence. It is reported in Ref. 39 that the damage in the optical material is established once the temperature of the defect-surrounding material reaches its melting point. Therefore, threshold fluence as a function of this critical temperature (melting point of the optical material, which, in our case, is silica) can be now estimated as

$$F_0 = \frac{3.1\,T_c K_h \sqrt{\tau}}{\gamma \sqrt{D}} = 2.8 \text{ J/cm}^2, \tag{3}$$

where F_0 is the threshold damage fluence, T_c is the critical temperature or the melting point of silica ≈1900 K, K_h is the thermal conductivity = 1.4 W/(mK), τ is the pulse duration = 10 ps, D is the thermal diffusivity (for silica) = 0.0075 cm^2/s, and γ is the absorptivity at 1053 nm = 10^{-3}.

Therefore, the LIDT of the gratings can be normalized to F_0. The dimensional plot shown earlier in Fig. 146.26 is replotted in Fig. 146.33 by using dimensionless quantities. This plot may be used to ascertain the trend that, for increasing fracture strains, the normalized laser-induced–damage fluence will also increase. As the correlating lines pass through the origin, the implication is that high brittleness would lead to very low LIDT.

Conclusions

A novel analysis has been presented to show that nano-indentation testing, supported by SEM images and finite-element simulations, can be effectively used to interpret the quality of a grating post-cleaning. The most widely accepted metrics to rate the performance of MLD gratings used in

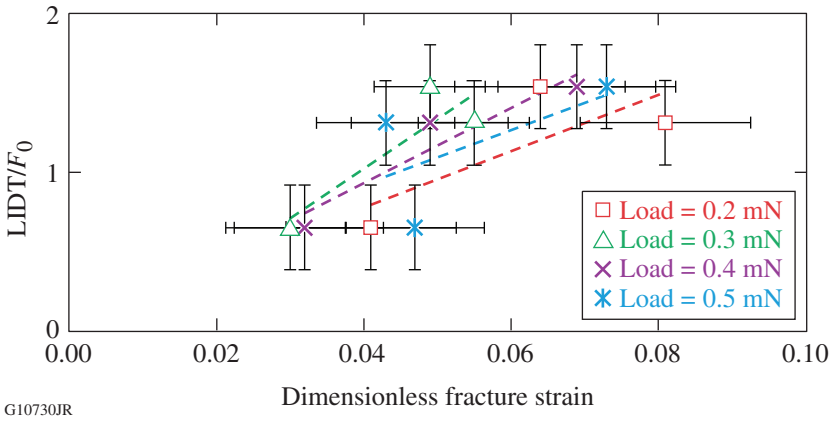

Figure 146.33
Normalized plot showing the dependence of damage thresholds on fracture strain developed in gratings during nano-indentation testing.

high-powered laser systems are expressed through optical tests in the form of LIDT's. Not only do nanomechanical tests naturally complement laser-damage testing by providing a fracture-derived metric (Δ_{min}) that distinguishes between grating samples based on their propensity to fracture, but they also expose identical regions of the grating structure to stresses as in a laser-damage test. The analogy is illustrated in Fig. 146.34. Therefore, we have argued that nanomechanical testing carried out in the proposed way (that is, identifying the weakest mode of the grating deformation) can be implemented as a rapid first test to predict how MLD gratings will perform when subjected to more-rigorous and specialized optical tests such as laser-damage testing.

In Fig. 146.34, we summarize schematically the analogy between stress/strain field concentration and electromagnetic-field concentration.

The main conclusions from this study are as follows: (1) Subtle changes in grating cleaning techniques lead to significant changes in the measured LIDT. (2) Our work shows a strong correlation between the nanomechanical fracture-based metric Δ_{min} and LIDT measured through optical testing for the grating samples evaluated. It is observed that a smaller value of LIDT is associated with a smaller Δ_{min} or, simply, a grating that has a tendency to fracture easily in a nano-indentation test will most likely have the lowest laser-damage threshold. (3) LIDT decreases as the measured yield stress for the grating samples increases. In other words, the less-deformable gratings lead to reduced LIDT. (4) The presence and size of undulations, or surface heterogeneities, on the grating structure have a direct impact on how the grating performs in both mechanical and optical tests. A grating with severe disfigurement at the top of the wall is more likely to have a low value of LIDT, as compared to a grating that was relatively free of this artifact. (5) Off-centered nano-indentation and LIDT measurements expose the same regions of the structure of the MLD grating and, therefore, can be seen as complementary tests.

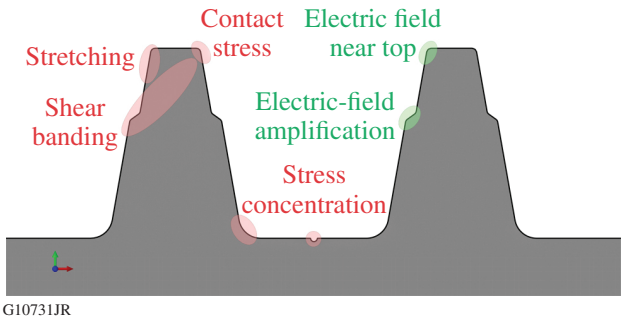

Figure 146.34
Nano-indentation exposes the same areas of the grating structure as an optical test by concentrating mechanical fields (stress, strain) in the regions normally associated with amplified electric fields.

In summary, we have presented a novel way of using nano-indentation testing, electron microscopy, and finite-element simulations to interpret the LIDT's of amorphous silica optical gratings.

ACKNOWLEDGMENT

The authors express their appreciation to the University of Rochester's Laboratory for Laser Energetics (LLE) for continuing support. One of the authors (K. Mehrotra) is supported by an LLE Horton Fellowship. This material is based upon work supported by the Department of Energy National Nuclear Security Administration under Award Number DE-NA0001944, the University of Rochester, and the New York State Energy Research and Development Authority. The support of DOE does not constitute an endorsement by DOE of the views expressed in this article.

The authors thank the late Dr. S. D. Jacobs for useful discussions that helped in conceiving this work. We also thank B. Patterson for her help in numerical simulations.

REFERENCES

1. F. Kong *et al*., Opt. Laser Technol. **73**, 39 (2015).
2. H. P. H. Liddell, "Enhancing the Performance of Multilayer-Dielectric Diffraction Gratings Through Cleaning Process Modifications and Defect Mitigation," Ph.D. thesis, University of Rochester, 2013.
3. D. Strickland and G. Mourou, Opt. Commun. **56**, 219 (1985).
4. G. A. Mourou, in *Encyclopedia of Modern Optics*, edited by R. D. Guenther, D. G. Steel, and L. P. Bayvel (Elsevier Academic Press, Amsterdam, 2005), pp. 83–84.
5. L. J. Waxer, D. N. Maywar, J. H. Kelly, T. J. Kessler, B. E. Kruschwitz, S. J. Loucks, R. L. McCrory, D. D. Meyerhofer, S. F. B. Morse, C. Stoeckl, and J. D. Zuegel, Opt. Photonics News **16**, 30 (2005).
6. J. A. Britten *et al*., Proc. SPIE **2714**, 511 (1996).
7. H. P. Howard, A. F. Aiello, J. G. Dressler, N. R. Edwards, T. J. Kessler, A. A. Kozlov, I. R. T. Manwaring, K. L. Marshall, J. B. Oliver, S. Papernov, A. L. Rigatti, A. N. Roux, A. W. Schmid, N. P. Slaney, C. C. Smith, B. N. Taylor, and S. D. Jacobs, Appl. Opt. **52**, 1682 (2013).
8. K. Mehrotra, H. P. Howard, S. D. Jacobs, and J. C. Lambropoulos, AIP Adv. **1**, 042179 (2011).
9. M. L. Schattenburg *et al*., the International Symposium on Nano-manufacturing (ISNM 2006), Cambridge, MA, 1–3 November 2006 (Paper TS3C-44).
10. J. R. Greer, W. C. Oliver, and W. D. Nix, Acta Mater. **53**, 1821 (2005).
11. J.-Y. Kim and J. R. Greer, Acta Mater. **57**, 5245 (2009).
12. J.-Y. Kim, D. Jang, and J. R. Greer, Acta Mater. **58**, 2355 (2010).
13. W. D. Nix *et al*., Thin Solid Films **515**, 3152 (2007).
14. R. Lacroix *et al*., International Journal of Applied Glass Science **3**, 36 (2012).
15. R. Lacroix *et al*., Acta Mater. **60**, 5555 (2012).
16. J. Neauport *et al*., Opt. Express **15**, 12508 (2007).
17. S. Hocquet, J. Neauport, and N. Bonod, Appl. Phys. Lett. **99**, 061101 (2011).
18. *LLE Review Quarterly Report* **112**, 228, Laboratory for Laser Energetics, University of Rochester, Rochester, NY, LLE Document No. DOE/SF/19460-790 (2007).
19. J. B. Oliver, T. J. Kessler, H. Huang, J. Keck, A. L. Rigatti, A. W. Schmid, A. Kozlov, and T. Z. Kosc, Proc. SPIE **5991**, 59911A (2005).
20. *LLE Review Quarterly Report* **131**, 149, Laboratory for Laser Energetics, University of Rochester, Rochester, NY, LLE Document No. DOE/NA/28302-1034 (2012).
21. H. T. Nguyen, C. C. Larson, and J. A. Britten, Proc. SPIE **7842**, 78421H (2010).
22. J. Keck, J. B. Oliver, T. J. Kessler, H. Huang, J. Barone, J. Hettrick, A. L. Rigatti, T. Hoover, K. L. Marshall, A. W. Schmid, A. Kozlov, and T. Z. Kosc, Proc. SPIE **5991**, 59911G (2005).
23. C. R. Wolfe *et al*., in *Laser Induced Damage in Optical Materials: 1989*, edited by H. E. Bennett *et al*., Natl. Inst. Stand. Technol. (U.S.), Spec. Publ. 801 (U.S. Government Printing Office, Washington, DC, 1990), pp. 360–375.
24. K. Mehrotra, H. P. Howard, S. D. Jacobs, and J. C. Lambropoulos, in *Local Probing Techniques and* In-Situ *Measurements in Materials Science*, edited by N. Balke *et al*., Mater. Res. Soc. Symp. Proc. Vol. 1474, mrss12-1474-ccc08-13 (Materials Research Society, Pittsburgh, PA, 2012).
25. K. Mehrotra, "Nano-Mechanics of Optical Structures for High Laser-Damage Threshold Applications," Ph.D. thesis, University of Rochester, 2016.
26. K. Mehrotra, J. B. Oliver, and J. C. Lambropoulos, Appl. Opt. **54**, 2435 (2015).
27. N. Bloembergen, Appl. Opt. **12**, 661 (1973).
28. Y. Jee, M. F. Becker, and R. M. Walser, J. Opt. Soc. Am. B **5**, 648 (1988).
29. A. Salleo *et al*., Proc. SPIE **3244**, 341–347 (1998).
30. F. Y. Génin *et al*., J. Opt. Soc. Am. A **18**, 2607 (2001).
31. S. Papernov and A. W. Schmid, J. Appl. Phys. **82**, 5422 (1997).
32. D. J. Smith *et al*., in *International Conference on Ultrahigh Intensity Lasers: Development, Science and Emerging Applications (ICUIL 2008)* (ICUIL, Tongli, China, 2008), pp. 78–79.
33. B. Ashe *et al*., Proc. SPIE **6720**, 67200N (2007).
34. B. Ashe, K. L. Marshall, C. Giacofei, A. L. Rigatti, T. J. Kessler, A. W. Schmid, J. B. Oliver, J. Keck, and A. Kozlov, Proc. SPIE **6403**, 64030O (2007).
35. S. Chen *et al*., Proc. SPIE **7655**, 765522 (2010).
36. S. Chen *et al*., High Power Laser Part. Beams **23**, 2106 (2011).
37. J. A. Britten *et al*., Proc. SPIE **5273**, 1 (2004).
38. B. C. Stuart *et al*., Proc. SPIE **2714**, 616–629 (1996).
39. S. Papernov, in *Laser-Induced Damage in Optical Materials*, edited by D. Ristau (CRC Press/Taylor & Francis, Boca Raton, FL, 2014), Sec. I, Chap. 3, pp. 25–74.